https://doi.org/10.1088/1361-6501/aa844a

Corrosion process monitoring by AFM higher harmonic imaging

S Babicz[1], **A Zieliński**[2], **J Smulko**[1] and **K Darowicki**[2]

[1] Faculty of Electronics, Department of Metrology and Optoelectronics, Telecommunications and Informatics, Gdańsk University of Technology, G. Narutowicza 11/12, 80-233 Gdańsk, Poland

[2] Faculty of Chemistry, Department of Electrochemistry, Corrosion and Materials Engineering, Gdańsk University of Technology, G. Narutowicza 11/12, 80-233 Gdańsk, Poland

Abstract

The atomic force microscope (AFM) was invented in 1986 as an alternative to the scanning tunnelling microscope, which cannot be used in studies of non-conductive materials. Today the AFM is a powerful, versatile and fundamental tool for visualizing and studying the morphology of material surfaces. Moreover, additional information for some materials can be recovered by analysing the AFM's higher cantilever modes when the cantilever motion is inharmonic and generates frequency components above the excitation frequency, usually close to the resonance frequency of the lowest oscillation mode. This method has been applied and developed to monitor corrosion processes. The higher-harmonic imaging is especially helpful for sharpening boundaries between objects in heterogeneous samples, which can be used to identify variations in steel structures (e.g. corrosion products, steel heterogeneity). The corrosion products have different chemical structures because they are composed of chemicals other than the original metal base (mainly iron oxides). Thus, their physicochemical properties are different from the primary basis. These structures have edges at which higher harmonics should be more intense because of stronger interference between the tip and the specimen structure there. This means that the AFM's higher-harmonic imaging is an excellent tool for monitoring surficial effects of the corrosion process.

Keywords: atomic force microscopy, higher-harmonic imaging, corrosion

1. Introduction

Steel is a very important construction material. Unfortunately, its quality and use is limited because of its heterogeneous structure, due to treatment and local corrosion effects. Costs of steel protection and conservation are very high [1]. Thus, it is important to test new alloys and protective coatings efficiently, quickly and accurately by observing even very subtle changes on their surfaces. In particular, inter-granular corrosion (IGC) [2] is very harmful for steel constructions and therefore requires careful attention to be identified at a preliminary stage [3]. Atomic force microscopy (AFM) [4] can be applied to analyse a metal surface in nanoscale, to recognize any changes in corrosion development and to understand its mechanism.

There exist many non-destructive testing and evaluation methods (NDE/NDT) in industry. In the field, we can note the use of optical coherence tomography (OCT) [5], impedance spectroscopy [6] and AFM diagnostics (e.g. dynamic impedance spectroscopy [7]). Previous works [8, 9] proved that higher-harmonic imaging [10] is very useful in examining heterogeneous samples [11] having very high- and low-amplitude topographic substructures. The image of a specimen created by higher harmonics can be used to gather information about the elastic properties of the specimen (i.e. its stiffness) [12]. Moreover, various substances are much easier to distinguish in non-homogeneous samples, because the higher-harmonic imaging enables clear differentiation of distinct materials [13, 14]. Higher harmonics can be even more sensitive when compared with conventional imaging. For example, inclusions in steel have different chemical structures because they are composed of chemicals other than the original metal base and should have slightly different stiffnesses.

Austenitic stainless steels (containing 18% chromium and 8% nickel) exhibit a high general and localized corrosion resistance. This is often the key factor in their selection to work in aggressive chemical environments, or in nuclear and conventional power plants (e.g. steam turbines), despite the relatively poor mechanical properties of these steels [15]. The good corrosion resistance results from the addition of chromium, with its protective effect observed when the content exceeds the critical value of 13%. On the other hand, the range of useful operating temperatures of the aforementioned steels is limited by the phenomenon of thermal sensitization leading to subsequent IGC attacks [16–18].

It is important to consider what type of chemical entities can be created on a steel surface. The physical properties of the arising products would determine possible applications of the higher-harmonic images. In the case of austenitic stainless steel, it is expected to be able to observe products of the passivation process [19] and possible passivity breakdown. An additional thermal sensitization process would lead to the appearance of intermetallic phases. In the latter case, it is assumed that exposure to temperatures in the range of 425–815 °C during welding or working lifetime leads to precipitation of carbides (such as $Cr_{23}C_6$) or intermetallic phases at the grain boundaries [20]. This phenomenon promotes the formation of chromium-depleted regions in their vicinity. $Cr_{23}C_6$ carbide is recognized to be responsible for local chromium depletion and thereby sensitization to IGC [20], which is observed when the chromium content falls below 12–13%. It should be noted that the thermal sensitization of austenitic steels is a process taking place in solid phase phenomena. The degradation of the material is the effect of the subsequent interaction with the liquid medium, governed by an electrochemical mechanism. The chromium-depleted grain boundary region is less resistant to corrosion than the interior of the grain. The preferential weld corrosion takes place at the grain boundaries while the interior of the grains remains passive. Thus, the higher-harmonic images could be used to monitor sensitization of steel by recognizing the differences at the grain boundaries.

Global mechanical properties and the corrosion resistance of alloys depend not only on their composition, but also on their structure. Heterogeneities play a special role in the structure of a material. Due to their energy level, which is different from that of the environment, they may constitute zones of accelerated corrosion or form cathodic areas which contribute to degradation of their surroundings. In the case of polycrystalline materials, the grain boundaries always constitute a place where such phenomena as surface diffusion, sedimentation and corrosion occur and have a significant influence on the macroscopic properties of the construction material [21]. Apart from heterogeneities, such as manganese sulphide inclusions forming during the metallurgical process, in the case of austenitic steel one also can observe intergranular generation of intermetallic compounds, which results from thermal sensitization. Depending on the conditions, carbides ($Cr_{23}C_6$), σ (Fe–Cr) and η (Fe2Mo) phases [20], nitrides (Cr_2N) [22], χ Laves phases or other compounds may form.

Yanliang *et al* [23] pointed out the economic advantages of Cr 13 steels compared to, for example, materials from the Cr 22 group. On the other hand, the former type is susceptible to thermal sensitization associated with inhomogeneities of its structure, eventually leading to corrosion cracking. The above situation makes the applicability of the described alloys limited until a complete understanding of the cracking mechanism is achieved. The authors demonstrate the ability to visualize precipitations by means of the AFM's dynamic mode. On the other hand, as the authors themselves stated, sensitization may lead to several products, depending on the material composition and the course of the process [13, 15]. Thus, the use of simple topographical imaging does not allow a selective identification of individual intermetallic compounds. In order to achieve selectivity of different types of protrusions/corrosion products, several attempts were taken.

Hakiki and Bubendorff [24] used the technique of a scanning Kelvin probe (SKPM) to demonstrate the existence of subtle changes in the Volta potential, which is one of the physicochemical characteristics of the oxide on the surface of high-alloy steel type 304 and 316. The presence of oxide layers has a key influence on the properties of the material similarly, as in the case of intermetallic compounds formed during thermal sensitization. For the described experiments (oxidation), the changes are small, at 30 mV/10 nm. In addition, the work confirms an increase in the Volta potential for phases enriched in chrome, which was confirmed by the work of Sathirashindy [25]. The application of a SKPM in corrosion research is related, however, to a number of problems such as the difference between the corrosion potential and the Volta potential, oxidation of the tip during the process, and the influence of topography on the result of the measurement. Hence, it is of value to create an alternative technique for the identification of different intermetallic phases present in the heterogeneous structures of construction materials.

2. Methodology

Controlling phenomena such as local corrosion in precisely defined conditions is the subject of many studies, including those formalized by normative documents such as ASTM G 108-94 (tests of intergranular corrosion of high-alloyed steels), ASTM G48-11 (2015) (pitting and crevice high-alloy steels) and ASTMG110-92 (corrosion of aluminum alloys). The mentioned techniques were used successfully in studies of industrial materials by means of an electrochemical-microscopic approach. The several successful realizations of probe microscopy research combined with electrochemical conditions of operation are listed below. The corrosion of aluminum alloy 2024 was analyzed via advanced *in situ* analytical tools [26]. Firstly, IR reflection–absorption spectroscopy enabled the identification of a pseudo-boehmite layer on the initial surface, which remained present also after the electrochemical treatment at different potentials. Secondly, formation of oxyhydroxides was confirmed by confocal

Raman spectroscopy. To get a deeper insight into the morphological changes, a three-electrode electrochemical AFM cell was utilised. The results of the measurements revealed an increase in the surface roughness and a change in the topography of intermetallic particles; corrosion deposits were also observed. Singh *et al* [27] shows the technique of controlled localized corrosion of nickel alloys. The result of the degradation of the metallic thin film formed originally by sputtering and then administered electrochemical passivation was monitored, among others, by an AFM. Pitting on samples was induced by a potentiostatic anodic polarization. The work of Sarvghad-Moghaddam *et al* [28] shows the results of microscopic examination of a junction of two metals prone to galvanic corrosion. The interface between copper and aluminum alloy AA3003 was the subject of a multitechnique approach. The research was carried out by means of a topographic AFM and scanning Kelvin probe, after immersion to 1 M HCl for 30 s. It was found that the areas initiating localized corrosion were well correlated with the regions of the greatest Volta potential difference on the surface of the investigated samples. A similar approach, using a scanning probe microscopy variant, namely a Kelvin probe, was used to study localized corrosion of aluminum 3xxx alloys [29], which have a technological importance as a raw material for vehicle radiators. Among other things, the *in situ* mapping of topography was performed using an AFM/SECM and potential through SKPM. In the first case, a solution of 20 mM NaCl and 2 mM KI was used. Chloride ions were used to initiate the process of pitting, iodide ion was used a redox mediator in this microscopy variant. AFM measurements were carried out in the conditions of open circuit potential. To get a picture of the processes preceding the formation of pits, SECM imaging was performed for different anodic polarizations from open circuit to 200 mV. Thanks to these measurements, an insight into the phenomenon of localized corrosion and creation of corrosion products around the active sites, such as inclusions and grain boundaries, was obtained. Mapping using a Kelvin probe helped confirm the cathodic character of intermetallic phases relative to the aluminum matrix. The work of Sudesh *et al* [30] focused on the economically important phenomenon of localized corrosion of high-alloyed steels. It recognized that the presence of manganese sulphide inclusions contribute to an intensification of pitting corrosion on the surface of high-alloy steels. However, the mechanism of the occurrence of this phenomenon is still not fully understood. The authors used an *in situ* AFM in conjunction with an electrochemical system in order to visualize the pitting initiation in real time. The study used a potentiostatic mode AFM under anodic polarization at a concentration of 0.028 M of chloride ions. Martin's team work [31] focused on *in situ* monitoring of the behavior of 304 l steel in an aqueous medium containing chloride (borate buffer, $\text{pH} = 7.56$ with 0.5 M Cl^-) by means of electrochemical AFM. They investigated zones of pitting initiation under potentiodynamic control. The aim of this study was to determine pit distribution on a nanometer scale. It was found that the phenomenon concentrates itself at grain boundaries and stechiometric inhomogenities present in the material. The impact of the material treatment (including hardening resulting from the mechanical polishing) to the frequency of pit initiation was also taken into account. Williford *et al* [32] presented the result of applying ECAFM for imaging of the pit formation process as well as the development of intergranular corrosion. Studies were conducted in 1000 ppm NaCl and 1 M oxalic acid using potentiodynamic polarization. The use of sequential methods of imaging of the surface showed the course of initiation and early stages of the types of attack described in the work. Li [33] studied the phenomenon of the passivation of iron surfaces in wet air and electrochemical conditions (borate buffer: 0.0375 M sodium tetraborate, and 0.15 M boric acid, $\text{pH} = 8.4$). The formation of a passive layer during cyclic polarization was monitored; EC-AFM was used as a visualization tool. A significant heterogeneity of the resulting oxide film was observed, with the formation of local structures composed of $\gamma\text{Fe}_2\text{O}_3$ characterized by electrochemical activity. It was assumed that they were products of localized corrosion, formed at defects in the crystal lattice of the material. In the studies of Wang [34] droplets of dilute sulfuric acid applied on the surface of a high-alloy steel, AISI 304, were tested in a non-contact mode AFM, while the effect of their impact on the material was tested in contact AFM, photoelectron spectroscopy (XPS) and wavelength dispersive x-ray spectroscopy (WDXS). Microdroplets of the corrosive medium were imaged using a dynamic, non-contact mode AFM, even with no voltage applied between the probe and the sample surface. Investigations revealed two forms of the presence of corrosive media, namely microdroplets and microfilms. In areas covered by films, small amounts of corrosion products appeared and no formation of pits was observed. Under the microdroplets, the formation of pits was observed, which then are filled with corrosion products. Their structure and chemical composition was been confirmed by XPS and WDXS techniques.

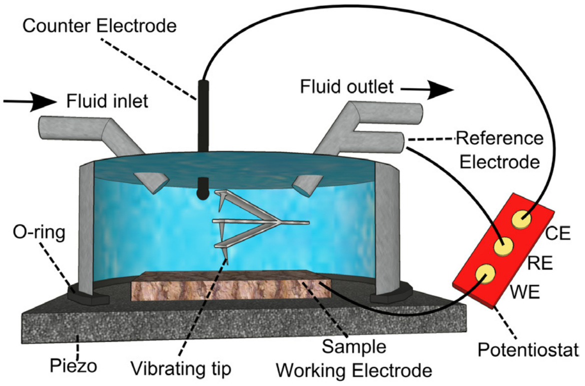

Figure 1. The measurement setup used for monitoring, by AFM, the corrosion of a specimen submerged in aqueous electrolyte.

The electrochemical (EC-AFM) experiment was performed using the NTegra Prima AFM by NT-MDT with an electrochemical adapter (figure 1). The examined specimen was austenitic steel AISI304. The specimen was subjected to temperature sensitization by heating for 1 h in 675 °C according to the ASTM standard. Before the AFM experiment, the specimen surface was prepared according to the following scheme. The specimen was subjected to wet grinding on sandpapers of increasing grade (400, 800, 1500 and 2000).

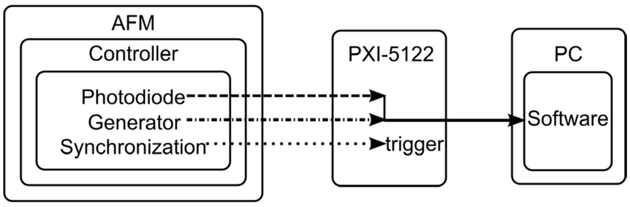

Figure 2. The measurement system scheme.

In each step, the specimen was ground on each side until a visually homogeneous surface was obtained. Then the specimen was rinsed with water with a surfactant and dried in a stream of hot air. The specimen was polished on a rotary polisher with a diamond suspension of decreasing size (15 μm, 9 μm and 3 μm). In each step the specimen was polished on each side for 15 min. Then the specimen was washed in an ultrasonic washer with deionized water and dried. Next, the specimen was polished with colloidal silica of 50 nm size and washed three times in the ultrasonic washer for 15 min, exchanging deionized water after each period. The specimen was completely immersed in 0.1 M solution of Na_2SO_4 to enable monitoring of the eventual corrosion development and scanned in intermediate contact mode. To observe the interaction between sample surface and electrolytic environment, periods of potentiostatic polarization were applied. An electrochemical three-electrode cell with a solid silver–silver chloride reference electrode was used. All polarizations discussed in the following part of the paper are expressed versus this electrode.

During measurement images of 256 × 256 pixels, covering the 25 μm × 25 μm austenitic steel area, were gathered. The resonance frequency of the applied cantilever was $f_0 = 206$ kHz. The measurement system used for higher-harmonic imaging was described in detail in previous works [8, 9]. During the scanning of the surface and its imaging by the dedicated AFM software, two signals were recorded by the data acquisition board: the reference sinusoidal signal exciting the cantilever with its resonance frequency, and the response signal from the photodiode (figure 2). The data acquisition board is triggered by the synchronization signal from the AFM, which enables division of the data during recording for separate parts corresponding to each pixel. The higher-harmonic images are created by software post-processing. The lock-in amplifier processes the recorded signals and determines the higher-harmonic (from the 1st to the 8th) level for each pixel separately. The maximum value of the sampling frequency, equal to 50 MSa s^{-1} for the PXI 5122 data acquisition board, assured over 800 periods (4.85 μs each) and more than 195.3 kSa of the excitation harmonic signal to characterize each pixel. The measurement scheme is presented in figure 3. The data were recorded at different corrosion stages, controlled by the applied polarizing voltage U_p. The initial images from the dedicated AFM software are presented in figure 4.

3. Results

The experiments, performed according to the measurement scheme (figure 3), resulted in obtaining numerous sets of pictures. This article considers only selected images representing the most valuable results, and those showing possible applications of higher harmonics in corrosion processes monitoring. In the presented images, intensities of the estimated consecutive higher harmonics were marked as S_n, where n is equal to their number.

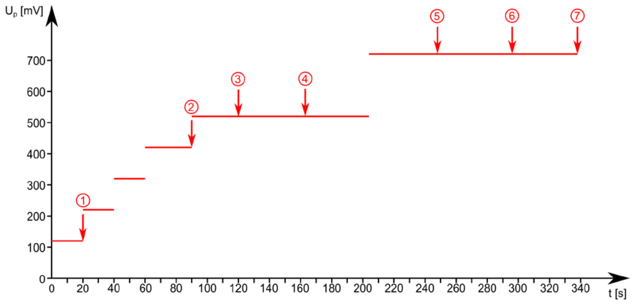

Figure 3. The measurement scheme of the applied anode polarizing voltage U_p versus time t; the measurement points 1, 2, 3, 4, 5, 6, 7 mark the moments of recording the AFM images; the polarizing voltage was switched off during specimen scanning.

The first sequence (figure 3, step 1) of the considered images was recorded after supplying a polarization of approximately 120 mV versus Ag/AgCl for 20 s. The lower parts of the pictures (figure 5) show signs of scratches left by the grinding process. There are also visible inclusions, which may be surficial structures or other compounds resulting from the process of thermal sensitization (especially in the upper parts of these pictures). This interpretation was established by considering experimental data obtained in similar laboratory experiments using an AFM or considering corrosion processes only. Cavities that could be associated with pitting corrosion processes were observed. It is worth mentioning that the image of the 2nd harmonic (figure 5(a)) has visible cavities at its lower part caused by the gridding process, whereas the image generated by the 7th harmonic (figure 5(b)) does not include such details.

The intensity bar in figures 5, 6 and 8–14 is presented in a greyscale within a range ⟨0; 255⟩ (left side) and responds linearly to the intensities of the selected higher harmonics estimated by the procedure presented elsewhere [35] (right side).

The next measurements (figure 3, step 2) were performed after applying a sequence of polarization voltages: 220 mV for 20 s, 320 mV for the next 20 s, and 420 mV for the last 30 s. The applied polarization conditions resulted in increasing the oxide layer coating of the specimen surface (figure 6); the height of the specimen slightly increased. It is worth noting that after the applied polarization voltages some objects had changed their size, for example the object at coordinates {23 μm, 21 μm} (figure 6(a)). This proves that the electrochemical processes resulted in developing corrosion products. The same effect of different sensitivity to different objects for various higher-harmonic images was observed as in the previous measurement phase (figure 3, step 1). The image generated for the second harmonic still has visible cavities (figure 6(a)), as reported in the previous stage (figure 5(a)), whereas the higher-harmonic images do not show such objects (e.g. the 4th harmonic image, figure 6(b)).

The next observations (figure 3, step 3), were performed after applying a polarization of 520 mV for 30 s. The results

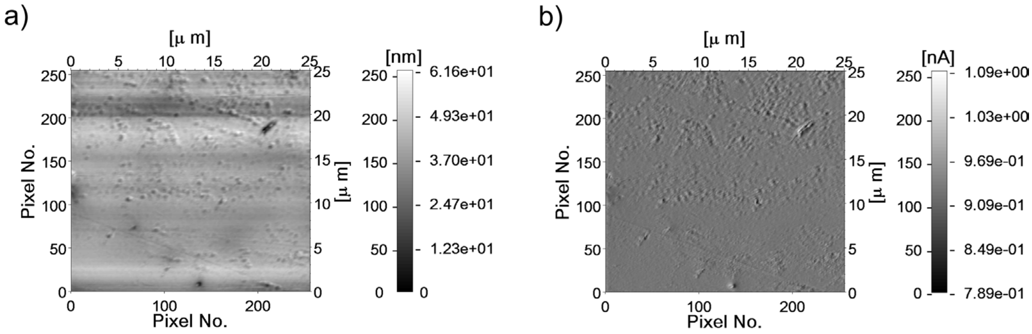

Figure 4. The initial surface of the AISI304 steel specimen generated by the NOVA software: (a) topography, (b) control error.

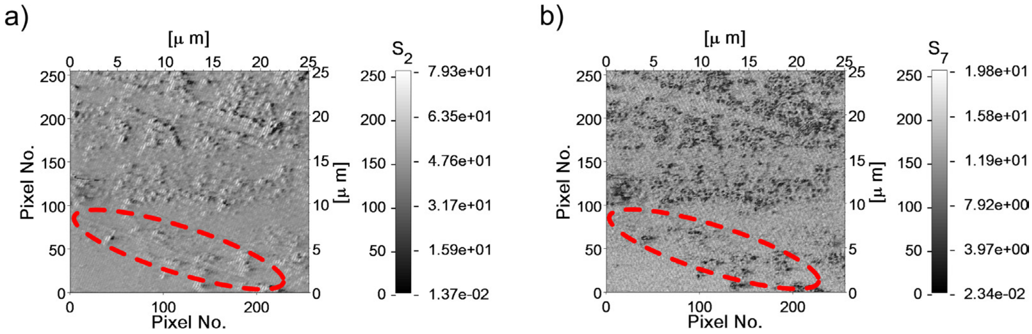

Figure 5. The higher-harmonic images of the AISI304 specimen surface in the first experiment phase: (a) the 2nd harmonic image, (b) the 7th harmonic image.

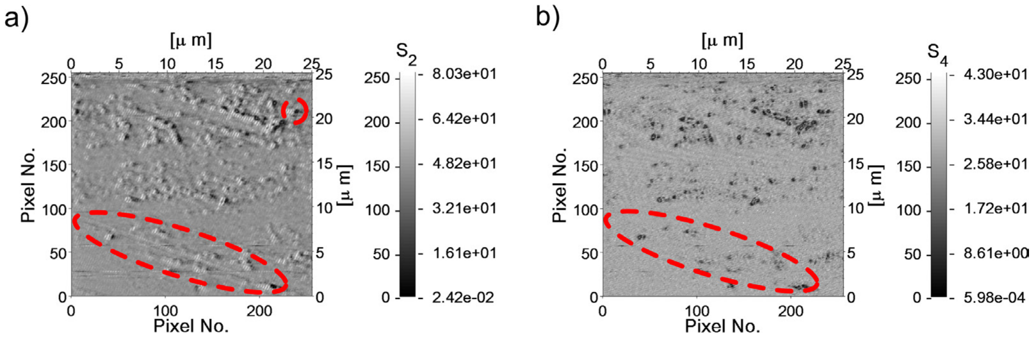

Figure 6. The higher-harmonic images of the AISI304 specimen surface in the second experiment phase: (a) the 2nd harmonic image, (b) the 4th harmonic image.

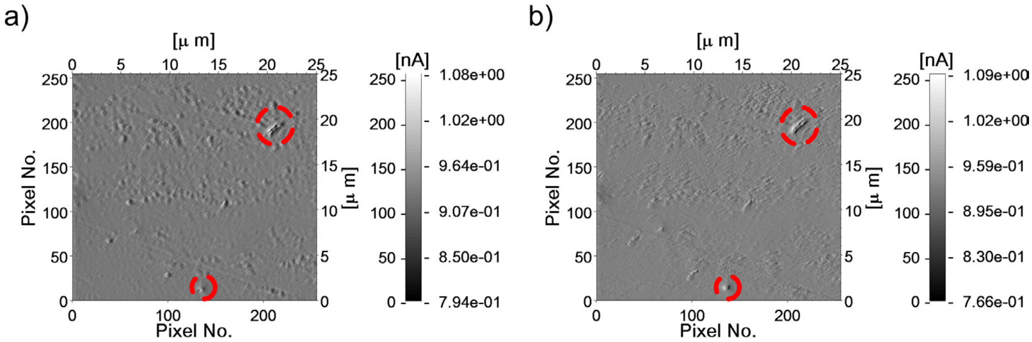

Figure 7. The control error images of the AISI304 specimen surface: (a) in the second experiment phase, (b) in the third experiment phase.

(figure 7(b)) exhibit two new and opposite phenomena. The size of the pit at coordinates $\{21\ \mu\text{m}, 19\ \mu\text{m}\}$ was slightly reduced (figure 7). At the same time, the relative height of the inclusions has decreased. These effects can be explained by a progressive development of the oxide layer on the surface of the steel electrode. On the other hand, a possible advancement of pitting in the lower part of image $\{14\ \mu\text{m}, 1\ \mu\text{m}\}$ is observed (figure 7). Moreover, the previously described difference (figure 6) between the 2nd harmonic image and the 4th (or 7th) harmonic images was still observed (figure 8).

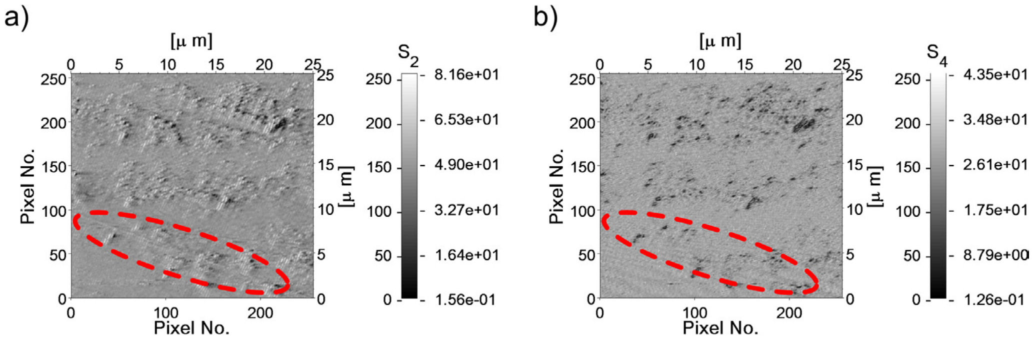

Figure 8. The higher-harmonic images of the AISI304 specimen surface in the third experiment phase: (a) the 2nd harmonic image, (b) the 4th harmonic image.

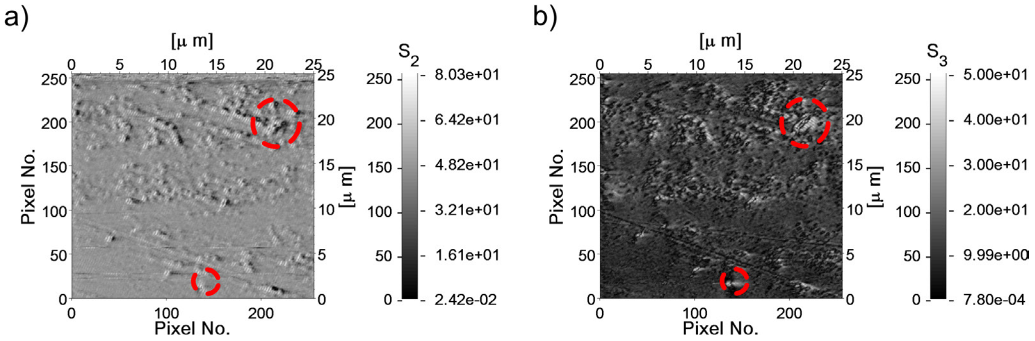

Figure 9. The higher-harmonic images of the AISI304 specimen surface in the fourth experiment phase: (a) the 2nd harmonic image, (b) the 3rd harmonic image.

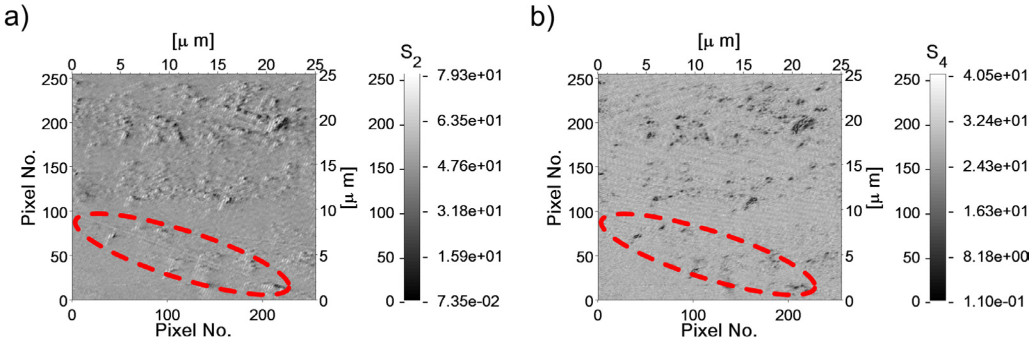

Figure 10. The higher-harmonic images of the AISI304 specimen surface in the fourth experiment phase: (a) the 2nd harmonic image, (b) the 4th harmonic image.

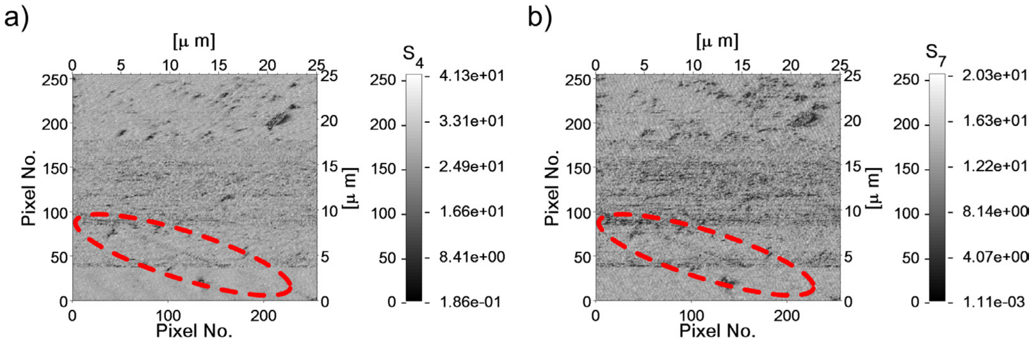

Figure 11. The higher-harmonic images of the AISI304 specimen surface in the fifth experiment phase: (a) the 1st harmonic image, (b) the 7th harmonic image.

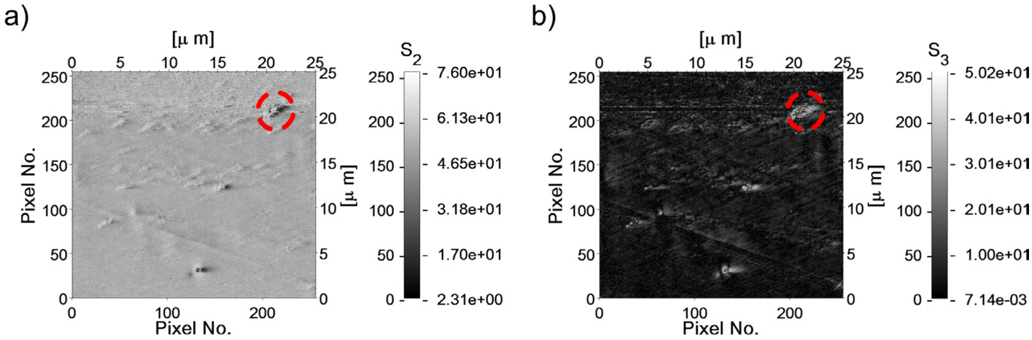

Figure 12. The higher-harmonic images of the AISI304 specimen surface in the sixth experiment phase: (a) the 2nd harmonic image, (b) the 3rd harmonic image.

The next measurements (figure 3, step 4) were performed after applying a polarization of 520 mV for 43 s. Further alignment of the surface was observed. This is consistent with the hypothesis of an increase of the oxide layer induced by the anodic polarization. The higher-harmonic images revealed a further increase of the pits at coordinates $\{21\ \mu\mathrm{m}, 19\ \mu\mathrm{m}\}$ and $\{14\ \mu\mathrm{m}, 1\ \mu\mathrm{m}\}$ (figure 9). A difference between the 2nd harmonic image and the 4th (or 7th) harmonic images was again observed (figure 10).

The next measurements (figure 3, step 5), were performed after applying a sequence of polarization voltages: 520 mV for 43 s and 720 mV for the last 43 s. The results (figure 11) exhibit a behaviour specific to the 4th harmonic image, exposing scratches made during the polishing procedure (figure 11(a)). The image of the 7th harmonic (figure 11(b)) also reveals these scratches but their exposition is weaker than in the previous case of the 4th component.

A next phase of corrosion development (figure 3, step 6) was observed after applying a polarization of 720 mV for 44 s. Further pit development at coordinates $\{21\ \mu\mathrm{m}, 19\ \mu\mathrm{m}\}$ was observed (figure 12). The pit increased so much that its shape changed. We can conclude that the generated images are quite selective for the mentioned pits (e.g. the images of the 2nd and the 3rd harmonics, figure 12).

The final phase of data recording (figure 3, step 7) was performed after applying a polarization of 720 mV for 45 s. The growth of the oxidation layer around the whole examined area was observed again. The cavities resulting from the surface treatment are still visible in the 4th harmonic image, as was noticed in the previous measurement phase (figure 13). The greatest difference between the images generated by higher harmonics was observed for the pit developed at coordinates $\{21\ \mu\mathrm{m}, 19\ \mu\mathrm{m}\}$ (figure 14). We observe that the object becomes very blurred at higher harmonics (e.g. the 7th harmonic, figure 14(b)). It can be concluded that the corrosion products cover the pit and that further development of corrosion processes should occur there.

4. Discussion

The presented measurement method enables the prediction of corrosion process development faster than typical surface analysis. The experiment proved the assumption that higher-harmonics imaging is very sensitive to charges

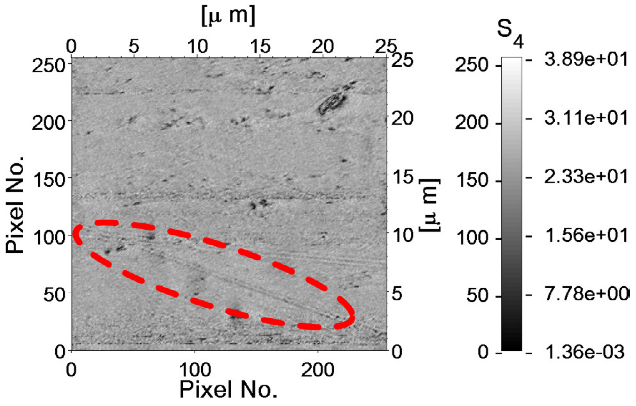

Figure 13. The 4th higher-harmonic image of AISI304 specimen in the 7th measurement point.

cumulated around the topographic substructures or local stiffness changes. The presented experimental results confirm that the intensity of the higher-harmonics of the tip's vibrations reveals additional information about the objects located at the investigated specimen. It should be underlined that it is difficult to determine which of the harmonics is more informative. Additionally, various objects can be exposed in a different way in consecutive images, so that it is impossible to select the most informative higher-harmonic. The unpredictable character of higher-harmonic behaviour enforces recording many, sometimes redundant, images. The final selection of images is the responsibility of the user. The opinion of the user is always individual and subjective. All these aspects make the method difficult to automate, like all methods relating to images.

There may occur a suspicion that polarization voltage affects the measurement. Therefore polarization voltage is always switched off during scanning. Otherwise, applied polarization can disturb the measured oscillations by introducing an additional voltage between the surface and the scanning tip. The extra current load in the tip–sample interaction would make it impossible to clearly observe corrosion effects that could arise in the higher-harmonic imaging. Moreover, the polarity must be switched off during signal recording to stabilize measurement conditions. Another point is that the scanning phase takes about 4.5 min, so that there would be an unacceptable difference in time of exposure to various corrosion agents during data acquisition for the first and the last pixels of the image. It is worth mentioning that the applied polarization caused not only a degradation of the examined

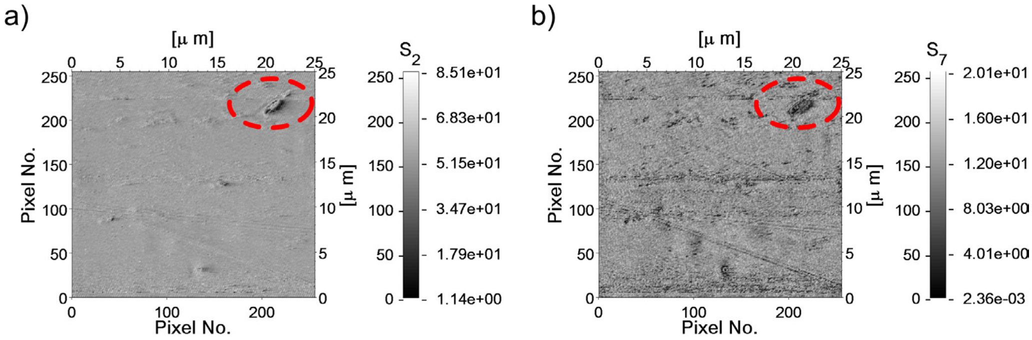

Figure 14. The AISI304 specimen with marked different fragments of the higher-harmonic images in the 7th measurement point: (a) the 2nd harmonic image, (b) the 7th harmonic image.

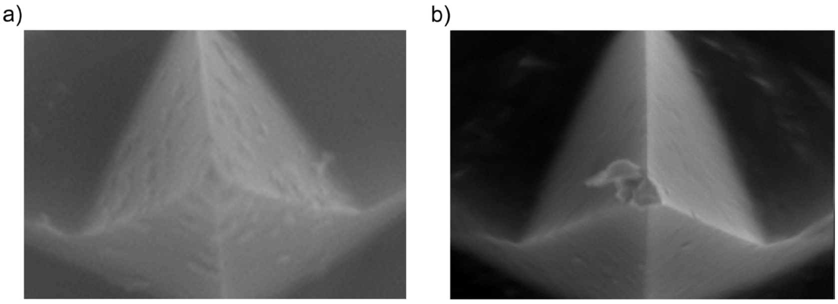

Figure 15. The NSG01 tip: (a) before EC-AFM measurements, (b) after 30 EC-AFM measurements of the 0.1 V polarization.

surface, but also caused damage to the scanning tip (figure 15). Unfortunately, changing probe each time after scanning can modify the measurement conditions. To minimize the effect of probe destruction it is necessary to use them only for a limited number of EC-AFM measurements. Additionally, it is worth checking the degree of degradation after each experiment series and eliminating the probes unfit for reuse.

The experimental results suggest that higher harmonics can expose some differences in examined heterogeneous structures with significantly different physical properties of their components (e.g. mechanical properties of glass fibre embedded in resin). In each measurement series, the higher-harmonic images have a better contrast than the images generated by the NOVA software. The experimental results proved that higher-harmonic images can characterize the topography of objects very selectively. The 4th and the 7th harmonics are more sensitive to extreme (high or low) topographic substructures, which can explain the invisibility of the polishing scratches in the 4th harmonic images.

The paper focuses on showing the possibility of extending traditional AFM imaging with a procedure which is sensitive to the presence of surficial structures of behavior differing from the matrix material. According to the works of [10], it is expected that the mentioned heterogeneities should generate a polyharmonic response that should vary with changing local mechanical properties. The possibility of differentiating such properties of materials can give way both to qualitatively delineating particular regions (such as carbide precipitates) and identifying different substances (steel matrix, oxide layer, intermetallic phases). The heterogeneity of the structure of a material has a major impact on a number of its properties. These include mechanical parameters [36], electrical conductivity [37] and corrosion resistance [38, 39]. Typically inhomogeneities or inclusions in the metal structure are characterized by different physical characteristics of the matrix material. This fact justifies the need to both distinguish between different types of chemical entities by microscopic analysis and also to predict the behavior of heterogeneous material structures on a macroscopic scale [21]. One example is the phenomenon of the sensitization of austenitic stainless steel to intergranular corrosion [40], due to segregation of alloy elements and the formation of intermetallic compounds followed by local depletion of the material component providing steel passivity. Xie's work [36] showed an atomic structure analysis of carbides produced by the abovementioned process. Using the techniques of computational chemistry, the crystal structure and thermodynamic properties of carbides were estimated, providing what is a promising methodology for the analysis of complex structures of this type of intermetallic phases.

5. Conclusions

The differences between higher-harmonic images during corrosion product development were identified. This fact can be explained by the significantly different mechanical properties of steel and oxides resulting from corrosion. Corrosion phenomena caused growth of oxides and development of local pits, resulting in a heterogeneity of the examined surface (its locally different physical properties). These results confirmed that corrosion processes can be monitored by higher harmonics. The technique is innovative and original for this application.

The results of the experiment proved the usefulness of higher-harmonic imaging for increasing the capabilities of an AFM during corrosion process monitoring, by revealing subtler differences between the surficial objects. The presented data can be used in more efficient quality assessments of metal materials or methods of corrosion protection. The presented way of performing the measurements should reduce the time taken by the necessary experiments and the operating costs of developing new materials for construction or methods of corrosion protection.

References

[1] Smulko J, Darowicki K and Zielinski A 2006 Evaluation of reinforcement corrosion rate in concrete structures by electrochemical noise measurements *Russ. J. Electrochem.* **42** 546

[2] Darowicki K, Zielinski A and Kurzydlowski K J 2008 Application of dynamic impedance spectroscopy to atomic force microscopy *Sci. Technol. Adv. Material.* **9** 045006

[3] Artunow A, Darowicki K and Tobiszewski M T 2013 Electrical mapping of AISI 304 stainless steel subjected to intergranular corrosion performed by means of AFM–LIS in the contact mode *Corros. Sci.* **71** 37

[4] Binnig G and Quate C F 1996 Surface studies by scanning tunneling microscopy *Phys. Rev. Lett.* **49** 57

[5] Antoniuk P, Strąkowski M, Pluciński J and Kosmowski B 2012 Non-destructive inspection of anti-corrosion protective coatings using optical coherent tomography *Metrol. Meas. Syst.* **19** 365

[6] Hoja J and Lentka G 2013 A family of new generation miniaturized impedance analyzers for technical object diagnostics *Metrol. Meas. Syst.* **20** 43

[7] Ryl J, Bogdanowicz R, Slepski P, Sobaszek M and Darowicki K 2014 Dynamic electrochemical impedance spectroscopy (DEIS) as a tool for analyzing surface oxidation processes on boron-doped diamond electrodes *J. Electrochem. Soc.* **161** H359

[8] Babicz S, Smulko J and Zieliński A 2013 Enhancing capabilities of atomic force microscopy by tip motion harmonics analysis *Bull. Acad. Pol. Sci.* **61** 535

[9] Babicz S, Zieliński A, Smulko J and Darowicki K 2013 A measurement system for nonlinear surface spectroscopy with an atomic force microscope during corrosion process monitoring *Pomiary Autom. Kontrola* **59** 287

[10] Stark R W and Stark M 2000 *Applied Scanning Probe Methods II. NanoScience and Technology* (Berlin: Springer) p 1

[11] Stark R W and Heckl W M 2000 Fourier transformed atomic force microscopy: tapping mode atomic force microscopy beyond the Hookian approximation *Surf. Sci.* **457** 219

[12] Legleiter J, Park M, Cusick B and Kowalewski T 2006 Scanning probe acceleration microscopy (SPAM) in fluids: mapping mechanical properties of surfaces at the nanoscale *Proc. Natl Acad. Sci. USA* **103** 4813

[13] Kokawa H, Shimada M and Sato Y 2000 Grain-boundary structure and precipitation in sensitized austenitic stainless steel *JOM* **52** 34

[14] Preiner J, Tang J, Pastushenko V and Hinterdorfer P 2007 Higher harmonic atomic force microscopy: imaging of biological membranes in liquid *Phys. Rev. Lett.* **99** 046102

[15] Aydoğdu G H and Aydinol M K 2006 Determination of susceptibility to intergranular corrosion and electrochemical reactivation behaviour of AISI 316L type stainless steel *Corros. Sci.* **48** 3565

[16] Kokawa H, Shimada M, Michiuchi M, Wang Z J and Sato Y S 2007 Arrest of weld-decay in 304 austenitic stainless steel by twin-induced grain boundary engineering *Acta Mater.* **54** 5401

[17] Gaudett M A and Scully J R 1993 Distributions of Cr depletion levels in sensitized AISI 304 stainless steel and its implications concerning intergranular corrosion phenomena *J. Electr. Soc.* **140** 3425

[18] Kelly W K, Iyer R N and Pickering H W 1993 Another grain boundary corrosion process in sensitized stainless steel *J. Electr. Soc.* **140** 3134

[19] Kerner Z, Horvath A and Nagy G 2007 Comparative electrochemical study of 08H18N10T, AISI 304 and AISI 316L stainless steels *Electrochim. Acta* **52** 7529

[20] Sahlaoui H, Makhlouf K, Sidhom H and Philibert J 2004 Effects of ageing conditions on the precipitates evolution, chromium depletion and intergranular corrosion susceptibility of AISI 316L: experimental and modeling results *Mater. Sci. Eng.* A **372** 98

[21] Michiuchi M, Kokawa H, Wang Z J, Sato Y S and Sakai K 2006 Twin-induced grain boundary engineering for 316 austenitic stainless steel *Acta Mater.* **54** 5179

[22] Lopez N, Cid M and Puiggali M 1997 Application of double loop electrochemical potentiodynamic reactivation test to austenitic and duplex stainless steels *Mater. Sci. Eng.* A **229** 123

[23] Yanliang H, Kinsella B and Becker T 2008 Sensitisation identification of stainless steel to intergranular stress corrosion cracking by atomic force microscopy *Mater. Lett.* **62** 1863

[24] Maachi B, Pirri C, Mehdaoui C, Hakiki N E and Bubendorff J L 2011 Atomic force microscopy, scanning Kelvin probe force microscopy and magnetic measurements on thermally oxidized AISI 304 and AISI 316 stainless steels *Corros. Sci.* **53** 984

[25] Sathirachinda N, Pettersson R and Pan J 2009 Depletion effects at phase boundaries in 2205 duplex stainless steel characterized with SKPFM and TEM/EDS *Corros. Sci.* **51** 1850

[26] Kreta A, Rodošek M, Slemenik Perše L, Orel B, Gaberšček M and Šurca Vuk A 2016 *In situ* electrochemical AFM, ex situ IR reflection–absorption and confocal Raman studies of corrosion processes of AA 2024-T3 *Corros. Sci.* **104** 290

[27] Singh S, Basu S, Poswal A K, Tokas R B and Ghosh S K 2009 Electrochemically controlled pitting corrosion in Ni film: a study of AFM and neutron reflectometry *Corros. Sci.* **51** 575

[28] Sarvghad-Moghaddam M, Parvizi R, Davoodi A, Haddad-Sabzevar M and Imani A 2014 Establishing a correlation between interfacial microstructures and corrosion initiation sites in Al/Cu joints by SEM–EDS and AFM–SKPFM *Corros. Sci.* **79** 148

[29] Davoodi A, Pan J, Leygraf C and Norgren S 2007 Integrated AFM and SECM for in situ studies of localized corrosion of Al alloys *Electrochim. Acta* **52** 7697

[30] Sudesh Wijesinghe T L L and Blackwood D J 2007 Real time pit initiation studies on stainless steels: the effect of sulphide inclusions *Corros. Sci.* **49** 1755

[31] Martin F A, Bataillon C and Cousty J 2008 *In situ* AFM detection of pit onset location on a 304L stainless steel *Corros. Sci.* **50** 84

[32] Williford R E, Windisch C F and Jones R H 2000 *In situ* observations of the early stages of localized corrosion in Type 304 SS using the electrochemical atomic force microscope *Mater. Sci. Eng.* A **288** 54

[33] Li J and Meier D J 1998 An AFM study of the properties of passive films on iron surfaces *J. Electroanal. Chem.* **454** 53

[34] Wang R 2004 An AFM and XPS study of corrosion caused by micro-liquid of dilute sulfuric acid on stainless steel *Appl. Surf. Sci.* **227** 399

[35] Kiwilszo M and Smulko J 2009 Pitting corrosion characterization by electrochemical noise measurements on asymmetric electrodes *J. Solid State Electrochem.* **13** 1681

[36] Lütjering G 1998 Influence of processing on microstructure and mechanical properties of $(\alpha+\beta)$ titanium alloys *Mater. Sci. Eng.* A **243** 32

[37] Zieliński A, Bogdanowicz R, Ryl J, Burczyk L and Darowicki K 2014 Local impedance imaging of boron-doped polycrystalline diamond thin films *Appl. Phys. Lett.* **105** 131908

[38] Ryl J, Wysocka J, Jarzynka M, Zielinski A, Orlikowski J and Darowicki K 2014 Effect of native air-formed oxidation on the corrosion behavior of AA 7075 aluminum alloys *Corros. Sci.* **87** 150

[39] Ryl J, Wysocka J, Slepski P and Darowicki K 2016 Instantaneous impedance monitoring of synergistic effect between cavitation erosion and corrosion processes *Electrochim. Acta* **203** 388

[40] Ryl J, Wysocka J and Darowicki K 2014 Determination of causes of accelerated local corrosion of austenitic steels in water supply systems *Constr. Build. Mater.* **64** 246